



Theoretical analysis of high-order harmonic generation in liquids by a semiclassical methodJia-Xiang Chen  and Xue-Bin Bian **State Key Laboratory of Magnetic Resonance and Atomic and Molecular Physics, Wuhan Institute of Physics and Mathematics, Innovation Academy for Precision Measurement Science and Technology, Chinese Academy of Sciences, Wuhan 430071, China*

(Received 12 January 2023; accepted 3 April 2023; published 11 April 2023)

The study of high-order harmonic generation in liquid-state materials is still in its infancy. Quantitative models are highly required to understand the mechanisms. Here we develop a semiclassical method to investigate the ultrafast electron dynamics in liquids under monochromatic and two-color laser fields in momentum space. By assuming that different k values are decoupled, we construct a quasienergy band for the liquid model and give the group velocity of the ionized electrons under the driving field. It successfully predicts the caustic enhancement of the liquid harmonic spectrum. We also find that the cutoff of the liquid harmonic spectrum is determined by the k -dependent band gap. Our results provide a different perspective for analyzing the nonlinear and nonperturbative liquid-state harmonic generation.

DOI: [10.1103/PhysRevA.107.043111](https://doi.org/10.1103/PhysRevA.107.043111)**I. INTRODUCTION**

High-order harmonic generation (HHG) in condensed matter induced by intense lasers is an attractive phenomenon [1,2]. It has been utilized as a tool for the observation and manipulation of ultrafast electron dynamics [3–5] and the all-optical reconstruction of the energy band structure in crystals [6–9]. The origin of crystal HHG includes intraband Bloch oscillations [10–12] and interband polarizations [13–17], and the latter leads to the appearance of plateaus in HHG spectra, which can be well described by the three-step model [18,19]: (i) birth of electron-hole pairs, (ii) acceleration of electron-hole pairs under the laser field, and (iii) recombination of electron-hole pairs and radiation of high-order harmonics.

Recently, HHG from liquids opened a new avenue for tracking ultrafast liquid-state dynamics [20–25]. The maximum coherent travel distance [26] and the cask theory [25] were introduced to account for the dependence of the maximum high-order harmonic radiation energy on the laser intensity and wavelength. However, due to the complexity of liquids, current theories of liquid HHG still lack an efficient description for the semiclassical trajectory of electrons, that is, the ionized-electron motion under the driving field. In addition, a novel phenomenon in the HHG spectrum of liquid-state water is that the first plateau cutoff energy is independent of laser parameters [24], which is never seen in either gas or solid HHG.

Semiclassical trajectory is a crucial tool for analyzing the spectra of gas and solid HHG and was successfully applied to predict the cutoff frequency [19,27–29] and the interference fringe [30–33] for the HHG spectrum, which is expected to extend to liquid HHG. The ionized electrons in liquids are affected by both the driving field and the Coulomb interaction of the surrounding atoms. Thus, like in solids, we need the

group velocity to describe the mean trajectory of electrons in liquids. The radial distribution function (RDF) is a crucial fingerprint of liquids. It is fixed for the same material at equilibrium; therefore, the behavior of laser-driven electrons satisfies specific statistical laws when the Born-Oppenheimer approximation is employed. In other words, the RDF of liquids contains statistical information about the electronic structure, which may be used to construct the dispersion relation of the electron and give the group velocity of electrons under the driving field.

In the present work, based on the tight-binding (TB) model, the harmonic generation from a one-dimensional liquid model is studied by numerically solving the time-dependent Schrödinger equation (TDSE) in real space and analyzed with a semiclassical calculation. We first present the dependence of cutoff energy for liquid HHG spectrum on the laser intensity and wavelength by our model. Then we show the feasibility of analyzing liquid HHG by the semiclassical theory from the following two points. (i) The cutoff frequency of the harmonic spectrum is determined by the k -dependent band gap. (ii) The caustics enhancement pattern in the liquid HHG spectrum, which is quite sensitive to the semiclassical trajectory, is successfully predicted by the semiclassical theory.

This paper is organized as follows. In Sec. II, the theoretical model and basic equations are presented. The results are reported and discussed in Sec. III, and a brief summary is presented in Sec. IV. Atomic units (a.u.) are always used unless otherwise specified.

II. METHOD**A. Structure and basic equations**

We use a statistical random atomic-chain model to simulate the liquid HHG process [26]. The schematic of a simple two-band TB model for the atomic chain is shown in Fig. 1(a)

*xuebin.bian@wipm.ac.cn

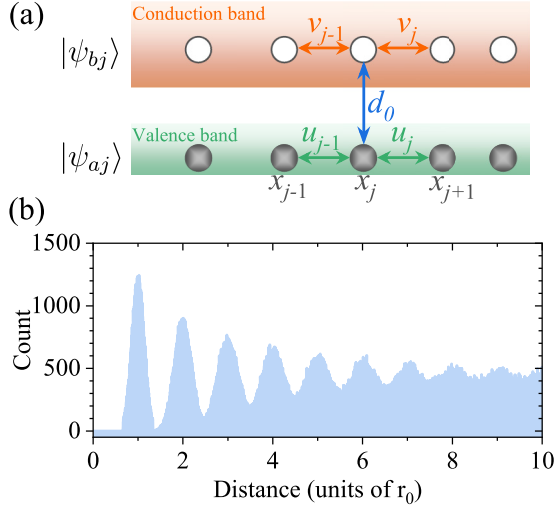


FIG. 1. (a) Schematics of the one-dimensional liquid model. The filled and unfilled circles at the j th atom site (x_j) represent two orbitals of the same atom, $|\psi_{aj}\rangle$ and $|\psi_{bj}\rangle$, respectively. u_j and v_j are the hopping integral from atom j to $j+1$ and their value is determined by the atomic spacing $r_j = x_{j+1} - x_j$ [see Eq. (2)]. d_0 is the transition dipole moment between two states for the same atom. (b) The histogram of the distance between all atom pairs.

and more details of the statistical random model can be found in Ref. [26]. In this model, the electronic structure of the atomic chain can be represented as a linear combination of two atomic orbitals per atom $|\phi_{a,j}\rangle$ and $|\phi_{b,j}\rangle$ [see in Fig. 1(a)]. Thus, the time-dependent Hamiltonian of the two-band TB model in real space has the following form:

$$\begin{aligned}
 H(t) = & \Delta_a \sum_{j=1}^N a_j^\dagger a_j + \Delta_b \sum_{j=1}^N b_j^\dagger b_j + \sum_{j=1}^{N-1} u_j (a_j^\dagger a_{j+1} + \text{H.c.}) \\
 & - \sum_{j=1}^{N-1} v_j (b_j^\dagger b_{j+1} + \text{H.c.}) - F(t) \sum_{j=1}^N x_j (a_j^\dagger a_j + b_j^\dagger b_j) \\
 & - d_0 F(t) \sum_{j=1}^N (a_j^\dagger b_j + \text{H.c.}), \quad (1)
 \end{aligned}$$

where N denotes the hopping range and x_j labels the j th atom site. a_j (b_j) is the annihilation operator referring to the valence (conduction) band; Δ_a and Δ_b are the on-site energies of the two bands. $d_0 = \langle \phi_{a,j} | x | \phi_{b,j} \rangle$ is the transition dipole moment between different states for the same atom [see blue arrows in Fig. 1(a)], which is independent of the atomic spacing. $F(t)$ is the electric field of the laser, with $F(t) = F_0 \cos(\omega_0 t) f(t)$, where $f(t)$ is trapezoidal with five cycles at peak intensity (3-5-3). u_j (v_j) is the hopping integral between $|\phi_{a,j}\rangle$ ($|\phi_{b,j}\rangle$) and $|\phi_{a,j+1}\rangle$ ($|\phi_{b,j+1}\rangle$). Specifically, to achieve short-ranged hopping, we adopt a modified scaling such that

$$\begin{aligned}
 u(r) &= u_0 \exp[-(r - r_0)/8], \\
 v(r) &= v_0 \exp[-(r - r_0)/8]. \quad (2)
 \end{aligned}$$

Here, $u_j = u(r_j)$ and $v_j = v(r_j)$, where $r_j = x_{j+1} - x_j$. The spacing r_j between two adjacent atoms satisfies the truncated normal distribution with an average spacing r_0 and the

corresponding distribution function of atomic spacing is shown in Fig. 1(b), which reflects the short-range order and long-range disorder of liquids [34,35].

The field-free Hamiltonian has $2N$ eigenstates $|\psi_i(t=0)\rangle = \sum_j (\phi_{a,j}^\dagger a_j^\dagger + \phi_{b,j}^\dagger b_j^\dagger) |0\rangle$ with $i = 1, 2, \dots, 2N$, where $\phi_{m,j}$ is the value of the electronic wave function in the atomic orbital $|\phi_{m,j}\rangle$ ($m = a, b$ and $j = 1, 2, \dots, N$) and $|0\rangle$ is a vacuum state. In the simulation of liquid HHG, we consider that the electrons initially occupy the first N bound eigenstates. The TDSE is solved for $|\psi_i(t)\rangle$ by applying the fourth-order Runge-Kutta method with a time step $\Delta t = 0.0093$ a.u.

Considering the disorder of the atoms in liquids, we average the HHG spectra of M random short atomic chains instead of a single long atomic chain. The HHG spectra obtained by this treatment converge faster and were employed in our previous work [36]. Here, each random short atomic chain has the same statistical distribution function of atomic spacing. Then the current for the m th chains reads

$$J_m(t) = -\frac{d}{dt} \sum_{i=1}^N \langle \psi_i^m(t) | x | \psi_i^m(t) \rangle. \quad (3)$$

Thus the spectrum of HHG can be written as the absolute square of the Fourier-transformed (FT) current

$$I(\omega) = \frac{1}{M} \left| \sum_m \mathcal{F}[J_m(t)] \right|^2. \quad (4)$$

In the simulation of liquid HHG, we follow the authors of Ref. [26] and choose $r_0 = 10$ a.u. It is close to the average spacing of liquid ethanol (about 8.7 a.u.) and liquid isopropanol (about 9.5 a.u.) at room temperature. The bandwidth of the conduction band is generally larger than that of the valence band and here we set their ratio to 3, that is, $v_0 = 3u_0$. The on-site energy for the valence band is $\Delta_a = 0$ a.u. and for the conduction band is $\Delta_b = 0.75$ a.u. While we choose $v_0 = 0.17$ a.u., the band gap of our model is about 0.3 a.u. and close to the band gap of common liquids, such as liquid water (about 0.32 a.u.). The value of the transition dipole moment d_0 does not affect the plateau cutoff energy of the HHG spectrum, and here we set $d_0 = 0.7$ a.u. However, our findings are not specific to this choice of model parameters.

B. k space

We transform the TDSE from the real space to k space for analyzing the mechanism of liquid HHG. To achieve this purpose, we introduce the transform $a_j^\dagger = \frac{1}{\sqrt{N}} \sum_k \exp(-ikx_j) a_k^\dagger$ together with $K = k - A(t)$, and then the time-dependent Hamiltonian can be rewritten as

$$\begin{aligned}
 \tilde{H}(t) = & \sum_{K,K'} \{ [\Delta_a f_S(\kappa_t, \kappa'_t) + f_u(\kappa_t, \kappa'_t)] a_K^\dagger a_{K'} \\
 & + [\Delta_b f_S(\kappa_t, \kappa'_t) - f_v(\kappa_t, \kappa'_t)] b_K^\dagger b_{K'} \\
 & - d_0 F(t) [f_S(\kappa_t, \kappa'_t) a_K^\dagger b_{K'} + \text{H.c.}] \}, \quad (5)
 \end{aligned}$$

where $\kappa_t = K + A(t)$. The structure factors

$$f_S(k, k') = \frac{1}{N} \sum_j e^{i(k-k')x_j}, \quad (6)$$

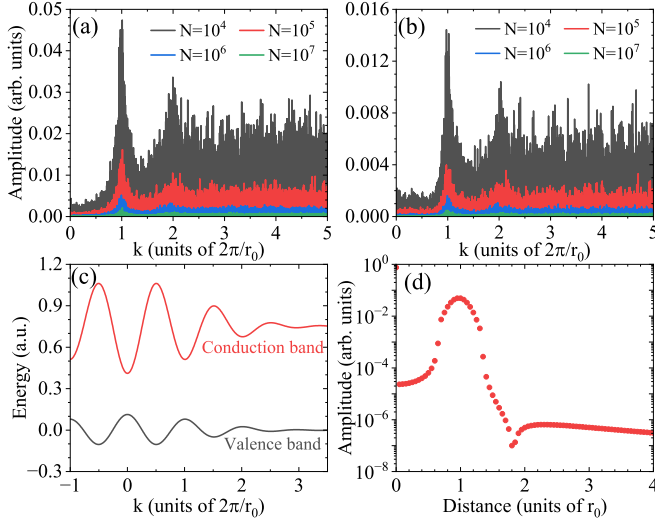


FIG. 2. Dependence of structure factors (a) $f_S(k, k' = 0)$ and (b) $f_u(k, k' = 0)$ on k value for $N = 10^4, 10^5, 10^6, 10^7$ (from top to bottom), respectively. (c) The quasienergy band structure of our one-dimensional liquid model. (d) Fourier transformation of the conduction band.

and

$$f_h(k, k') = \frac{1}{N} \sum_j h_j e^{-i(k'-k)x_j + ikr_j} + \text{c.c.}, \quad (7)$$

where $h = u, v$ and the vector potential $A(t) = -\int_{-\infty}^t F(\tau) d\tau$.

The structure factors $f_S(k, k' = 0)$ for several N are shown in Fig. 2(a) except for the point $k = 0$ where the value is 1, independent of N . Here we note that $f_S(k, k' = 0)$ decreases as N increases. For every tenfold increase in N , $f_S(k, k' = 0)$ becomes about one-third of the original. The case of f_u is similar to that of f_S and is shown in Fig. 2(b). So for a large N , coupling between different k values can be approximately regarded as a perturbation and ignored, that is, $f_S(k, k') \approx \delta_{k,k'}$ and

$$\begin{aligned} f_h(k, k') &\approx f_h(k) \delta_{k,k'} \\ &= \frac{\delta_{k,k'}}{N} \sum_j h_j e^{ikr_j} + \text{c.c.} \\ &= \frac{\int h(r) \exp(ikr) g(r) dr}{\int g(r) dr} \delta_{k,k'} + \text{c.c.}, \end{aligned} \quad (8)$$

where the hopping term $h_j = h(r_j)$ ($h = u, v$), and $g(r)$ is the spacing distribution function for nearest-neighbor atom pairs, namely, the first peak in Fig. 1(b).

With the above approximations, Eq. (5) no longer depends on the arrangement of atoms in the statistical random chain but instead on $g(r)$. Thus, the probability amplitude $\alpha_v(K, t)$ for the valence band and $\alpha_c(K, t)$ for the conduction band in k space are coupled in the fashion

$$i \frac{\partial}{\partial t} \begin{pmatrix} \alpha_v(K, t) \\ \alpha_c(K, t) \end{pmatrix} = \begin{pmatrix} \varepsilon_v(\kappa_t) & -F(t)d_0 \\ -F(t)d_0 & \varepsilon_c(\kappa_t) \end{pmatrix} \begin{pmatrix} \alpha_v(K, t) \\ \alpha_c(K, t) \end{pmatrix}, \quad (9)$$

where the valence band $\varepsilon_v(k) = \Delta_a + f_u(k)$ and the conduction band $\varepsilon_c(k) = \Delta_b - f_v(k)$ are the two quasienergy bands

of Eq. (1) and shown in Fig. 2(c). Both quasienergy bands are symmetric with respect to $k = 0$. Compared with the crystalline band structure, those of the liquid system are non-periodic and the amplitude decays with increasing $|k|$, which is mainly determined by $g(r)$ and the hopping term. In the region where $|k| > 6\pi/r_0$, the two quasienergy bands can be regarded as flat bands, which represent the localized electron wave function in liquids. A broad peak at the average distance r_0 of the Fourier-transformed conduction band in Fig. 2(d) is due to the only consideration of the nearest-neighbor hopping and the nearest-neighbor atomic spacing with a truncated normal distribution.

Here, the solution of Eq. (9) is independent of the number of atomic chains M . The indirect transition is prohibited in Eq. (9), i.e., the electron transitions in different bands can only occur at the same k value. The transition dipole moment between the valence and conduction bands is independent of k values and is a constant d_0 . Hence, the interband current for a single K reads

$$J_{er}(K, t) = -d_0 \frac{\partial [\alpha_v^*(K, t) \alpha_c(K, t) + \text{c.c.}]}{\partial t}, \quad (10)$$

and the intraband current reads

$$J_{ra}(K, t) = -[|\alpha_v(K, t)|^2 p_v(\kappa_t) + |\alpha_c(K, t)|^2 p_c(\kappa_t)], \quad (11)$$

where $p_m(k) = \partial \varepsilon_m(k) / \partial k$. The total HHG spectrum can be written as $I(\omega) = |\mathcal{F}\{\sum_K [J_{ra}(K, t) + J_{er}(K, t)]\}|^2$.

We notice that Eq. (9) has the same form as the TDSE using the Houston states in crystals [15,37]. Following the semiclassical method developed for atomic and solid HHG [18,38,39], we introduce the transform $\alpha_m = \exp[-i \int_{-\infty}^t \varepsilon_m(\kappa_\tau) d\tau] \beta_m$ ($m = c, v$). Then Eq. (9) can be rewritten as

$$\dot{\beta}_v(K, t) = iF(t)d_0 \exp[-iS(K, t)] \beta_c(K, t), \quad (12)$$

$$\dot{\beta}_c(K, t) = iF(t)d_0 \exp[iS(K, t)] \beta_v(K, t), \quad (13)$$

where $S(K, t) = \int_{-\infty}^t \varepsilon_g(\kappa_\tau) d\tau$ and $\varepsilon_g = \varepsilon_c - \varepsilon_v$. We define the off-diagonal density matrix element $\Pi = \beta_v^* \beta_c$, and the corresponding differential equation

$$\dot{\Pi}(K, t) = iF(t)d_0 \exp[iS(K, t)] (|\beta_v|^2 - |\beta_c|^2). \quad (14)$$

$|\beta_v|^2 - |\beta_c|^2$ describes the population difference between the valence and conduction bands. For the convenience of analysis, the Keldysh approximation [40] ($|\beta_v|^2 - |\beta_c|^2 \approx 1$) is adopted and then inserted into Eq. (10). We have the interband harmonic

$$\begin{aligned} J_{er}(\omega) &= \int_{-\infty}^{\infty} dk \int_{-\infty}^{\infty} dt e^{-i\omega t} \int_{-\infty}^t dt' \\ &\quad \times G(t') e^{-iS(k, t', t)} + \text{c.c.}, \end{aligned} \quad (15)$$

where $G(t') = \omega d_0^2 F(t')$ and the classical action $S(k, t', t) = \int_{t'}^t \varepsilon_g[k - A(t) + A(\tau)] d\tau$.

III. RESULT AND DISCUSSIONS

This work focuses on the spectral cutoff and enhancement in liquid HHG. For our theoretical model described in Sec. II, we adopt the number of atomic chains $M = 100$ and each chain has $N = 512$ atoms. For the laser parameters used in

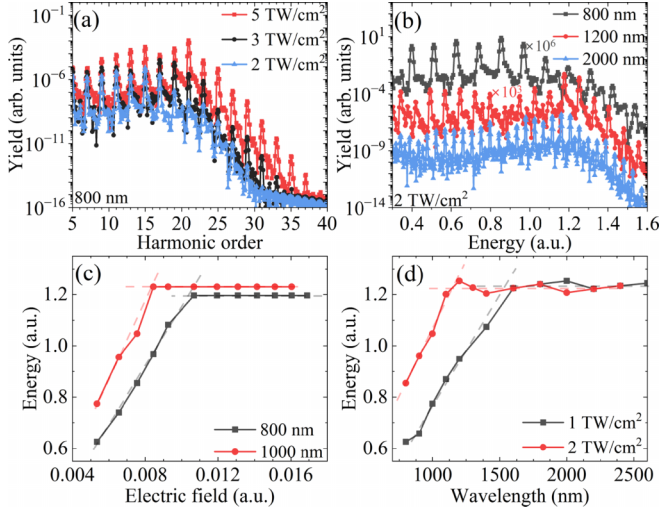


FIG. 3. (a) HHG spectra for laser intensities $I_0 = 2$ TW/cm² (blue triangles), 3 TW/cm² (black filled cycles), and 5 TW/cm² (red squares), respectively. (b) HHG spectra for laser wavelengths $\lambda = 800$ nm, 1200 nm, and 2000 nm (from top to bottom), respectively. Dependence of HHG cutoff on (c) electric strength and (d) wavelength. The dashed slashes are obtained by linear fit and the horizontal dashed lines are the average of the plateau data points. The inflection point of (c) electric strength or (d) wavelength are determined by the intersection of two dashed lines of the same color.

the numerical simulations, we verify that the HHG spectrum above the band gap remains almost unchanged if M or N is doubled.

A. Dependence of spectral cutoff on laser parameters

The HHG spectra for the carrier wavelength $\lambda = 800$ nm are shown for several laser field intensities in Fig. 3(a). As we can see, the spectral cutoff of HHG increases significantly when the laser intensity increases from 2 TW/cm² to 3 TW/cm². Whereas the spectral cutoff seems to saturate despite continuing to increase the laser intensity to 5 TW/cm². Figure 3(c) further demonstrates the dependence of the cutoff energy on the electric field strength for $\lambda = 800$ nm and $\lambda = 1000$ nm. Obviously, the relationship between the cutoff frequency (Ω_c) and F_0 can be divided into two parts: one is that Ω_c has a positive correlation with F_0 and the other is that Ω_c is independent of F_0 . The inflection point for $\lambda = 800$ nm is $F_0 \approx 0.010$ a.u. and for $\lambda = 1000$ nm it is $F_0 \approx 0.0084$ a.u. That is, the larger the wavelength, the smaller the field strength of the inflection point.

To further demonstrate the effect of laser parameters on the cutoff energy, the HHG spectra for $I_0 = 2$ TW/cm² are shown for several carrier wavelengths in Fig. 3(b). The corresponding wavelength dependence of the spectral cutoff is shown in Fig. 3(d). Similar to the field-strength-dependent cutoff energy, the spectral cutoff increases with the wavelength increase until saturation. The threshold value of wavelength is about 1540 nm for $I_0 = 1$ TW/cm² and about 1150 nm for $I_0 = 2$ TW/cm².

It should be reiterated that we are concerned with the cutoff of the HHG spectrum plateau rather than the

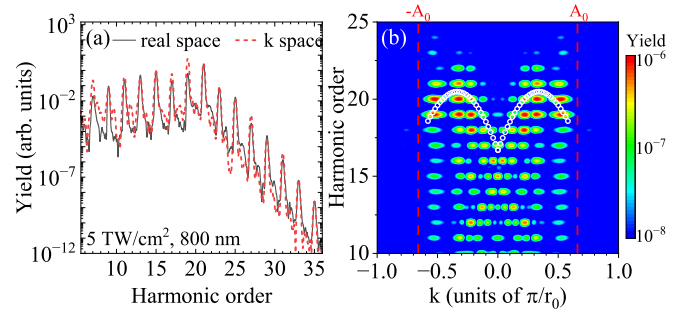


FIG. 4. (a) HHG spectra obtained by solving Eq. (9) (red dashed line). The black solid line is the same as the red squares in Fig. 3(a) for comparison. (b) HHG spectra corresponding to each k -value component in the red dashed line in (a). The white unfilled circles are predicted by $\varepsilon_g(|k| + A_0)$. The red dashed lines represent the position of $|k| = A_0$.

maximum harmonic radiation energy Ω_{\max} [24–26]; for example, $\Omega_{\max} = 37\omega_0$ when $I_0 = 5$ TW/cm². Ω_{\max} will be affected by the second conduction band if we consider more bands. Therefore, discussing Ω_{\max} is not meaningful in this work. In addition, we noted that the maximum cutoff energy is about 1.2 a.u. Specifically, the values of vector potential A_0 for all inflection points in Figs. 3(c) and 3(d) are close, about 0.18 ± 0.01 a.u. This value is relatively close to half of π/r_0 (0.16 a.u.), while those in crystal HHG are π/r_0 [19]. This inspires us that the spectral cutoff of the liquid HHG can be revealed in k space.

The HHG spectrum obtained by solving Eq. (9) for $I_0 = 5$ TW/cm² and $\lambda = 800$ nm is shown in Fig. 4(a) with the red dashed line and the red squares in Fig. 3(a) is shown again in Fig. 4(a) with solid black line for comparison. As we can see, the HHG spectra in k space have the same spectral structure as those in real space for the part where the spectrum energy is above the band gap. Specifically, they have the same cutoff frequency. That is, Eq. (9) can be used to analyze HHG spectrum in liquids.

The HHG spectrum in Fig. 4(a) (red dashed line) is the coherent superposition of the HHG spectrum for all k values. To analyze the source of the spectral cutoff, we show the HHG spectra resulting from each k value in Fig. 4(b). The two red dashed lines indicate $k = \pm A_0$, and the high-order harmonics for the initial k value in this interval dominate the total HHG spectrum. This is because the energy gap at point $k = 0$ is minimal. The electron-hole pairs are mainly born around that point and the motion range of electron-hole pairs in k space are $[k - A_0, k + A_0]$. In addition, the band gaps as a function of $|k| + A_0$ are indicated by the white unfilled circles in Fig. 4(b), which agree well with the spectral cutoff energy for a single k value. Thus, when $2A_0 < \pi/r_0$, the cutoff energy of the total HHG spectrum can be described by the spectrum for $k = \pm A_0$, namely, $\varepsilon_g(2A_0)$. That is, the threshold of the vector potential can be considered as half of π/r_0 .

B. Caustic enhancement

The harmonic spectrum above the minimum band gap is dominated by interband harmonics and can be described by Eq. (15). Similar to the treatment in the original recollision

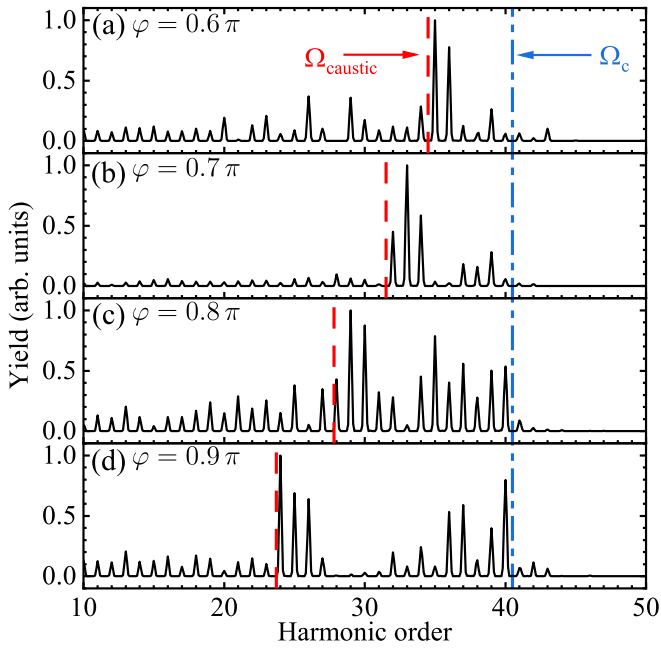


FIG. 5. (a) HHG spectra obtained by solving the real-space TDSE for phase delays $\varphi =$ (a) 0.6π , (b) 0.7π , (c) 0.8π , and (d) 0.9π , respectively. The red dashed lines and the blue dashed-dotted line represent the position of spectral caustics predicted by semiclassical calculations and the spectral cutoff, respectively. The selected parameters of the fundamental field are $F_0 = 0.0053$ a.u. (corresponding to the peak intensity of 1 TW/cm^2), frequency $\omega_0 = 0.03$ a.u., and ratio $R = 0.8$.

model [18,38], we assume that $G(t')$ is a slowly varying term. Applying the stationary phase method to the integration of Eq. (15), the electron-hole recollision model in liquids can be described by saddle-point conditions

$$\frac{\partial S(k, t_b, t_r)}{\partial k} = \int_{t_b}^{t_r} \frac{\partial \varepsilon_g[k - A(t_r) + A(\tau)]}{\partial k} d\tau = 0, \quad (16a)$$

$$\frac{\partial S(k, t_b, t_r)}{\partial t_b} = \varepsilon_g[k - A(t_r) + A(t_b)] = 0, \quad (16b)$$

$$\frac{\partial S(k, t_b, t_r)}{\partial t_r} = \varepsilon_g(k) = \Omega, \quad (16c)$$

where Ω is the harmonic energy, t_b and t_r represent the birth and recombination times of the electron-hole pairs, respectively.

To clarify the role of the semiclassical picture revealed by Eqs. (16a) to (16c) in the liquid HHG, we study the caustic enhancement of HHG which results from the coalescence of multiple branches of electron-hole trajectories [41–43]. A two-color laser field

$$A(t) = \frac{F_0}{\omega_0} \left[\sin(\omega_0 t) + \frac{R}{2} \sin(2\omega_0 + \varphi) \right] f(t), \quad (17)$$

is used here so that the caustic enhancement can be observed clearly and the caustic point in HHG spectrum can be adjusted by the phase delay φ .

Figures 5(a) to 5(d) show HHG spectra for several phase delays, which are obtained by solving the real-space TDSE,

namely, Eq. (1). As the phase delay changes from 0.6π to 0.9π , the harmonic order corresponding to the maximum value of the spectral plateau changes from 35th to 24th. The red dashed lines represent the position of the spectral caustics predicted by Eqs. (16a) to (16c) and $d\Omega/dt_b = 0$ [43]. As shown in Figs. 5(a) to 5(d), the caustic points predicted by the semiclassical calculation agree well with the enhancement in the harmonic spectra. Here, we need to point out that the caustic point in the semiclassical calculation represents the maximum recombination energy, not the cutoff frequencies of the harmonic spectrum. The cutoff frequency is about 40th-order harmonic and independent of phase delay [see the blue dashed-dotted line in Figs. 5(a) to 5(d)]. That is, the maximum recombination energy is always less than or equal to the cutoff energy, and the liquid HHG spectrum below the maximum recombination energy in the plateau can be described by the semiclassical theory.

IV. CONCLUSION

We numerically simulate and analyze the HHG spectrum in a simple but meaningful one-dimensional liquid model. In contrast to solving for the liquid cluster from time-dependent density function theory [44], this model provides the opportunity to neglect the weakly coupled terms so as to give an analytical expression of the harmonic spectrum in k space. It is advantageous for the analysis of liquid HHG mechanisms. After the establishment of the model, approximations are taken only in the k -space calculation. We show that the HHG spectrum obtained from the k -space calculation is similar in structure to that obtained from the real-space calculation in the spectral plateau and has the same cutoff frequency. In addition, we introduce the atomic spacing distribution function into the Hamiltonian of k space and give the quasienergy band structure and group velocity for the electron in liquids.

The results presented in this work reveal the dependence of cutoff in liquid HHG spectra on the laser parameters and demonstrate that applying solid-phase high-harmonic spectroscopy to liquids is possible. For example, we note that the cutoff frequency in the plateau of the liquid HHG spectrum is determined by the k -dependent band gap. By adjusting the phase delay of the two-color laser fields, the liquid HHG spectrum exhibits a distinct caustics enhancement pattern, similar to the solid HHG. Meanwhile, the position of spectral caustics contains the quasienergy band-structure information, which may provide a way to reconstruct the k -dependent band gap by spectral caustics [9]. Further work is needed to study the competition of different mechanisms in liquid HHG.

ACKNOWLEDGMENTS

J.-X.C. thanks A. Zeng, Z. Li, and C. Xia for helpful discussions. This work is supported by the National Natural Science Foundation of China (Grants No. 12247122 and No. 12274421), the CAS Project for Young Scientists in Basic Research (Grant No. YSBR-059), and the K. C. Wong Education Foundation (GJTD-2019-15).

- [1] S. Ghimire, A. D. DiChiara, E. Sistrunk, P. Agostini, L. F. DiMauro, and D. A. Reis, Observation of high-order harmonic generation in a bulk crystal, *Nat. Phys.* **7**, 138 (2011).
- [2] J. Q. Liu and X. B. Bian, Multichannel High-Order Harmonic Generation from Fractal Bands in Fibonacci Quasicrystals, *Phys. Rev. Lett.* **127**, 213901 (2021).
- [3] O. D. Mücke, Isolated high-order harmonics pulse from two-color-driven Bloch oscillations in bulk semiconductors, *Phys. Rev. B* **84**, 081202(R) (2011).
- [4] M. Schultze, E. M. Bothschafter, A. Sommer, S. Holzner, W. Schweinberger, M. Fiess, M. Hofstetter, R. Kienberger, V. Apalkov, V. S. Yakovlev, M. I. Stockman, and F. Krausz, Controlling dielectrics with the electric field of light, *Nature (London)* **493**, 75 (2013).
- [5] T. T. Luu, M. Garg, S. Y. Kruchinin, A. Moulet, M. T. Hassan, and E. Goulielmakis, Extreme ultraviolet high-harmonic spectroscopy of solids, *Nature (London)* **521**, 498 (2015).
- [6] G. Vampa, T. J. Hammond, N. Thiré, B. E. Schmidt, F. Légaré, C. R. McDonald, T. Brabec, D. D. Klug, and P. B. Corkum, All-Optical Reconstruction of Crystal Band Structure, *Phys. Rev. Lett.* **115**, 193603 (2015).
- [7] A. A. Lanin, E. A. Stepanov, A. B. Fedotov, and A. M. Zheltikov, Mapping the electron band structure by intraband high-harmonic generation in solids, *Optica* **4**, 516 (2017).
- [8] L. Li, P. Lan, L. He, W. Cao, Q. Zhang, and P. Lu, Determination of Electron Band Structure using Temporal Interferometry, *Phys. Rev. Lett.* **124**, 157403 (2020).
- [9] J. Chen, Q. Xia, and L. Fu, Reconstruction of crystal band structure by spectral caustics in high-order harmonic generation, *Phys. Rev. A* **104**, 063109 (2021).
- [10] S. Ghimire, A. D. Di Chiara, E. Sistrunk, G. Ndabashimiye, U. B. Szafruga, A. Mohammad, P. Agostini, L. F. DiMauro, and D. A. Reis, Generation and propagation of high-order harmonics in crystals, *Phys. Rev. A* **85**, 043836 (2012).
- [11] P. G. Hawkins and M. Y. Ivanov, Role of subcycle transition dynamics in high-order-harmonic generation in periodic structures, *Phys. Rev. A* **87**, 063842 (2013).
- [12] O. Schubert, M. Hohenleutner, F. Langer, B. Urbanek, C. Lange, U. Huttner, D. Golde, T. Meier, M. Kira, S. W. Koch, and R. Huber, Sub-cycle control of terahertz high-harmonic generation by dynamical Bloch oscillations, *Nat. Photonics* **8**, 119 (2014).
- [13] M. Korbman, S. Yu Kruchinin, and V. S. Yakovlev, Quantum beats in the polarization response of a dielectric to intense few-cycle laser pulses, *New J. Phys.* **15**, 013006 (2013).
- [14] M. Hohenleutner, F. Langer, O. Schubert, M. Knorr, U. Huttner, S. W. Koch, M. Kira, and R. Huber, Real-time observation of interfering crystal electrons in high-harmonic generation, *Nature (London)* **523**, 572 (2015).
- [15] M. Wu, S. Ghimire, D. A. Reis, K. J. Schafer, and M. B. Gaarde, High-harmonic generation from Bloch electrons in solids, *Phys. Rev. A* **91**, 043839 (2015).
- [16] Z. Guan, X. X. Zhou, and X. B. Bian, High-order-harmonic generation from periodic potentials driven by few-cycle laser pulses, *Phys. Rev. A* **93**, 033852 (2016).
- [17] Y. Kobayashi, C. Heide, H. K. Kelardeh, A. Johnson, F. Liu, T. F. Heinz, D. A. Reis, and S. Ghimire, Polarization flipping of even-order harmonics in monolayer transition-metal dichalcogenides, *Ultrafast Science* **2021**, 9820716 (2021).
- [18] G. Vampa, C. R. McDonald, G. Orlando, D. D. Klug, P. B. Corkum, and T. Brabec, Theoretical Analysis of High-Harmonic Generation in Solids, *Phys. Rev. Lett.* **113**, 073901 (2014).
- [19] G. Vampa, C. R. McDonald, G. Orlando, P. B. Corkum, and T. Brabec, Semiclassical analysis of high harmonic generation in bulk crystals, *Phys. Rev. B* **91**, 064302 (2015).
- [20] T. T. Luu, Z. Yin, A. Jain, T. Gaumnitz, Y. Pertot, J. Ma, and H. J. Wörner, Extreme-ultraviolet high-harmonic generation in liquids, *Nat. Commun.* **9**, 3723 (2018).
- [21] V. Svoboda, Z. Yin, T. T. Luu, and H. J. Wörner, Polarization measurements of deep- to extreme-ultraviolet high harmonics generated in liquid flat sheets, *Opt. Express* **29**, 30799 (2021).
- [22] Y. E. L. Zhang, A. Tsytkin, S. Kozlov, C. Zhang, and X.-C. Zhang, Broadband THz sources from gases to liquids, *Ultrafast Science* **2021**, 9892763 (2021).
- [23] O. Alexander, J. C. T. Barnard, E. W. Larsen, T. Avni, S. Jarosch, C. Ferchaud, A. Gregory, S. Parker, G. Galinis, A. Tofful, D. Garratt, M. R. Matthews, and J. P. Marangos, The mechanism of high harmonic generation in liquid alcohol, [arXiv:2202.12624](https://arxiv.org/abs/2202.12624).
- [24] A. Mondal, O. Neufeld, Z. Yin, Z. Nourbakhsh, V. Svoboda, A. Rubio, N. Tancogne-Dejean, and H. J. Wörner, Probing the low-energy electron-scattering dynamics in liquids with high-harmonic spectroscopy, [arXiv:2203.03617](https://arxiv.org/abs/2203.03617).
- [25] C. L. Xia, Z. L. Li, J. Q. Liu, A. W. Zeng, L. J. Lü, and X. B. Bian, Role of charge-resonance states in liquid high-order harmonic generation, *Phys. Rev. A* **105**, 013115 (2022).
- [26] A.-W. Zeng and X.-B. Bian, Impact of Statistical Fluctuations on High Harmonic Generation in Liquids, *Phys. Rev. Lett.* **124**, 203901 (2020).
- [27] T.-Y. Du and X.-B. Bian, Quasi-classical analysis of the dynamics of the high-order harmonic generation from solids, *Opt. Express* **25**, 151 (2017).
- [28] A. M. Parks, G. Ernotte, A. Thorpe, C. R. McDonald, P. B. Corkum, M. Taucer, and T. Brabec, Wannier quasi-classical approach to high harmonic generation in semiconductors, *Optica* **7**, 1764 (2020).
- [29] R. Zuo, A. Trautmann, G. Wang, W.-R. Hannes, S. Yang, X. Song, T. Meier, M. Ciappina, H. T. Duc, and W. Yang, Neighboring atom collisions in solid-state high harmonic generation, *Ultrafast Science* **2021**, 9861923 (2021).
- [30] T. Higuchi, C. Heide, K. Ullmann, H. B. Weber, and P. Hommelhoff, Light-field-driven currents in graphene, *Nature (London)* **550**, 224 (2017).
- [31] J.-Z. Jin, H. Liang, X.-R. Xiao, M.-X. Wang, S.-G. Chen, X.-Y. Wu, Q. Gong, and L.-Y. Peng, Michelson interferometry of high-order harmonic generation in solids, *J. Phys. B: At., Mol. Opt. Phys.* **51**, 16LT01 (2018).
- [32] H. Shirai, F. Kumaki, Y. Nomura, and T. Fuji, High-harmonic generation in solids driven by subcycle midinfrared pulses from two-color filamentation, *Opt. Lett.* **43**, 2094 (2018).
- [33] Y. W. Kim, T.-J. Shao, H. Kim, S. Han, S. Kim, M. Ciappina, X.-B. Bian, and S.-W. Kim, Spectral interference in high harmonic generation from solids, *ACS Photonics* **6**, 851 (2019).
- [34] J. L. Yarnell, M. J. Katz, R. G. Wenzel, and S. H. Koenig, Structure factor and radial distribution function for liquid argon at 85 °K, *Phys. Rev. A* **7**, 2130 (1973).

- [35] Z.-W. Ding, Y.-B. Wang, Z.-L. Li, and X.-B. Bian, High-order harmonic generation in liquids in bicircularly polarized laser fields, *Phys. Rev. A* **107**, 013503 (2023).
- [36] C.-L. Xia, J.-Q. Liu, L.-J. Lü, A.-W. Zeng, Z.-L. Li, and X.-B. Bian, Theoretical study of high-order harmonic generation in solutions, *J. Phys. B: At., Mol. Opt. Phys.* **55**, 045401 (2022).
- [37] C. Yu, S. Jiang, and R. Lu, High order harmonic generation in solids: A review on recent numerical methods, *Adv. Phys. X* **4**, 1562982 (2019).
- [38] M. Lewenstein, P. Balcou, M. Y. Ivanov, A. L'Huillier, and P. B. Corkum, Theory of high-harmonic generation by low-frequency laser fields, *Phys. Rev. A* **49**, 2117 (1994).
- [39] C. Qian, C. Yu, S. Jiang, T. Zhang, J. Gao, S. Shi, H. Pi, H. Weng, and R. Lu, Role of Shift Vector in High-Harmonic Generation from Noncentrosymmetric Topological Insulators under Strong Laser Fields, *Phys. Rev. X* **12**, 021030 (2022).
- [40] L. V. Keldysh, Ionization in the field of a strong electromagnetic wave, *Sov. Phys. JETP* **20**, 1307 (1965).
- [41] O. Raz, O. Pedatzur, B. D. Bruner, and N. Dudovich, Spectral caustics in attosecond science, *Nat. Photonics* **6**, 170 (2012).
- [42] A. J. Uzan, G. Orenstein, Á. Jiménez-Galán, C. McDonald, R. E. F. Silva, B. D. Bruner, N. D. Klimkin, V. Blanchet, T. Arusi-Parpar, M. Krüger, A. N. Rubtsov, O. Smirnova, M. Ivanov, B. Yan, T. Brabec, and N. Dudovich, Attosecond spectral singularities in solid-state high-harmonic generation, *Nat. Photonics* **14**, 183 (2020).
- [43] J. Chen, Q. Xia, and L. Fu, Spectral caustics of high-order harmonics in one-dimensional periodic crystals, *Opt. Lett.* **46**, 2248 (2021).
- [44] O. Neufeld, Z. Nourbakhsh, N. Tancogne-Dejean, and A. Rubio, Ab Initio cluster approach for high harmonic generation in liquids, *J. Chem. Theory Comput.* **18**, 4117 (2022).